Supporting Information

Multiscale modelling of charge transport in P3HT:DIPBI bulk heterojunction organic solar cells.

Tobias Koch, Jim Bachmann, Tobias Lettmann and Nikos L. Doltsinis[†]

[†] *Institut für Festkörpertheorie, Westfälische Wilhelms-Universität Münster and Center for Multiscale Theory & Computation, Wilhelm-Klemm-Str. 10, 48149 Münster, Germany; E-mail: nikos.doltsinis@wwu.de*

Contents

1 Segment chain length distribution

The distribution of the number of segments with a certain chain length distribution n are similar for the P3HT:DIPBI blend morphologies, when comparing different annealing schemes (500 K, 700 K, 900 K). Whereas, segments with $n = 1$ to 32 can occur in amorphous P3HT. In all cases the same cutoff dihedral angle $\theta^{\text{cut}}_{\text{SCCS}} = 75°$ is applied.

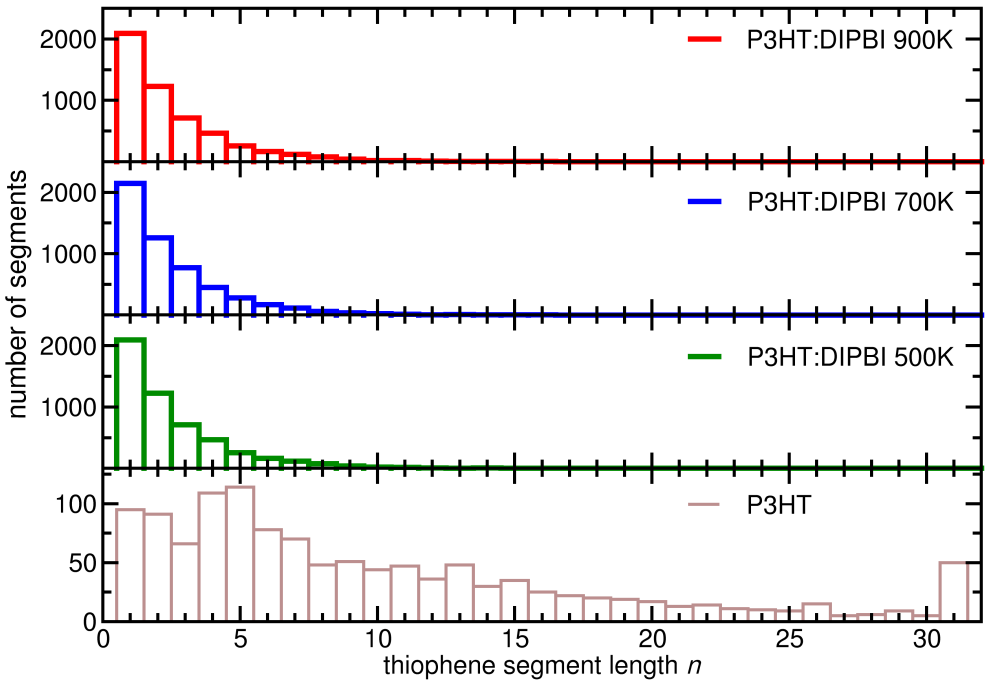

Figure S1: Distributions of the number of segments with a certain chain length distribution n for the P3HT:DIPBI blend after employing the polymer chain partitioning with $\theta^{\text{cut}}_{\text{SCCS}} = 75°$ in three different morphologies and CG annealing protocols [1] at 500 K, 700 K and 900 K in amorphous P3HT for comparison.

2 Internal reorganization energy λ^{in} and internal site energy difference ΔE^{in} based on DFTB

The internal reorganization energy λ_{in} and the internal site energy difference ΔE_{in} based on DFTB/Mio-1-1 are depicted in (Fig. S2) for heteromolecular DIPBI/P3MT and P3MT/DIPBI transitions. The DFTB data shows basically the same dependence of λ_{in} on the thiophene chain length n, as the DFT based data and can be extended to evaluate λ_{in} and ΔE_{in} up to $n = 32$. The $\lambda^{\text{h}}_{\text{in}}$ DFTB reorganization energies are about factor 5 and, than the corresponding data on B3LYP/6-311G** level of theory. The DIPBI / DIPBI $\lambda^{\text{h}}_{\text{in}} = 0.055$ eV is about half of the $\lambda^{\text{h}}_{\text{in}} = 0.130$ eV value. DIPBI / P3MT and P3MT/DIPBI transitions show similar trends for $\lambda^{\text{h}}_{\text{in}}$. In the long-chain limit the reorganization energies decay to $\lambda^{\text{h}}_{\text{in}} = 0.04$ eV.

Also $\Delta E_{\mathrm{in}}^{\mathrm{h}}$ (Fig. S2) exhibits similar trends as the corresponding DFT data (Fig. 2). In the long-chain limit the internal site energy difference tends towards $\Delta E_{\mathrm{in}}^{\mathrm{h}} = 2.33$ eV.

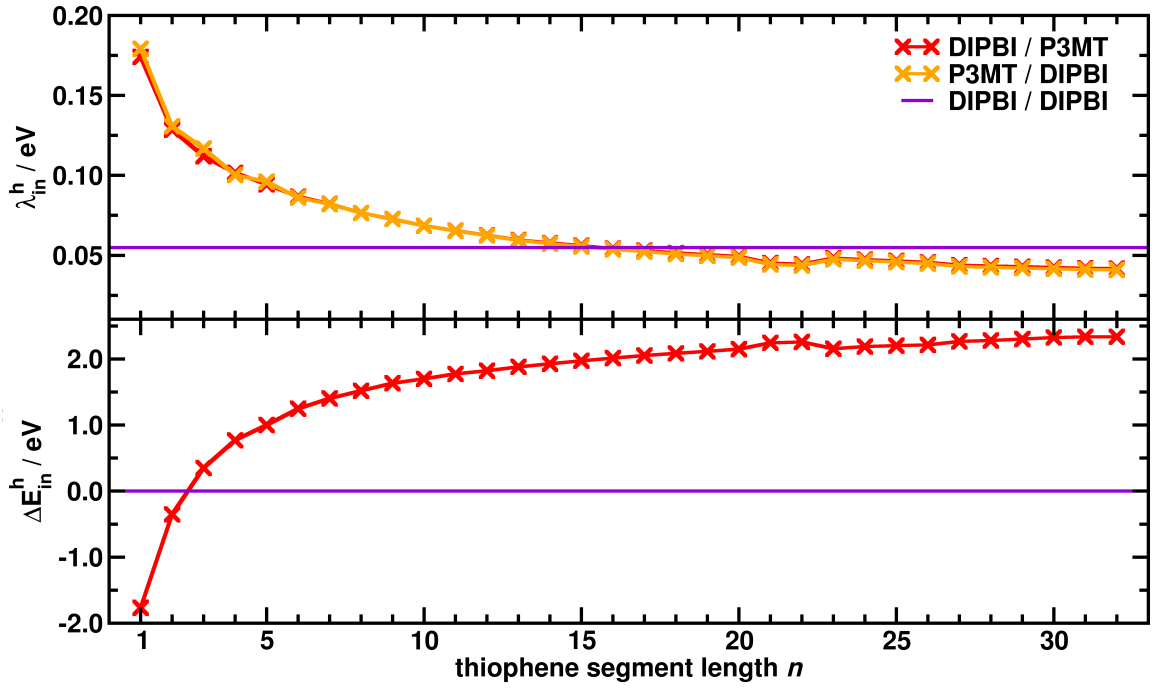

Figure S2: Internal reorganization energy $\lambda_{\mathrm{in}}^{\mathrm{h}}$ and internal site energy difference $\Delta E_{\mathrm{in}}^{\mathrm{h}}$ for hole transfer as a function of the number of tiophene units n in a P3MT chain. The data are based on DFTB/Mio-1-1. Transitions for hole transfer between DIPBI/P3MT (red), P3MT/DIPBI (orange) and DIPBI / DIPBI (violet) are taken into account. The sign of the internal site energy difference is reversed $\Delta E_{\mathrm{in}}^{\mathrm{h}}(\mathrm{AB}) = -\Delta E_{\mathrm{in}}^{\mathrm{h}}(\mathrm{BA})$, if the charge transfer is reversed.

3 Scaling the DIPRO charge transfer integral $|J_{AB}|$

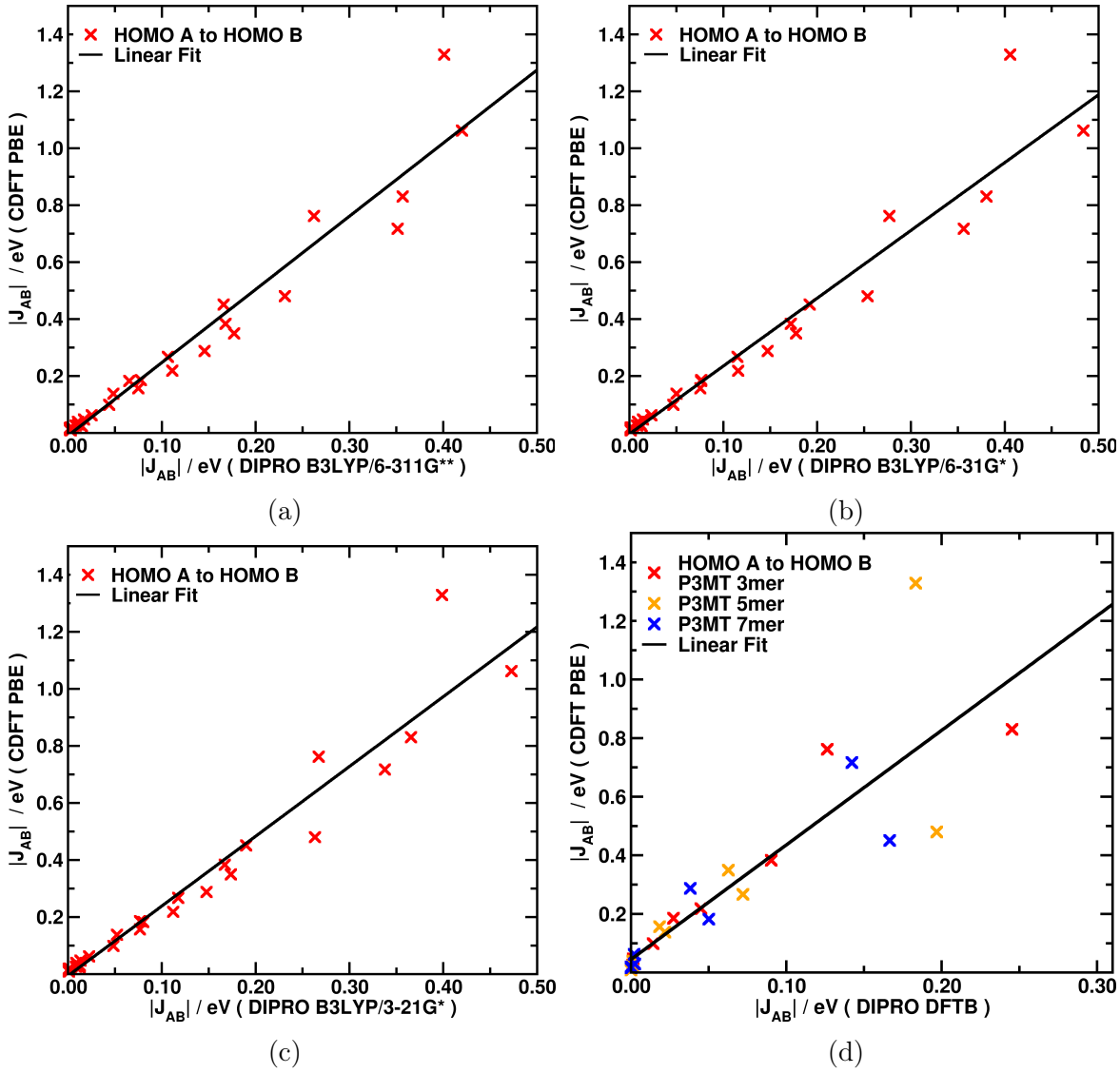

Figure S3: Basis set dependence of the charge transfer integral $|J_{AB}|$ for hole transport in pairs of P3MT $n = [3, 5, 7]$. The DIPRO data with (a) B3LYP/6-311G**, (b) B3LYP/6-31G*, (c) B3LYP/3-21G* are compared to the CDFT data on PBE/PW level of theory. (d) DFTB/Mio-1-1 is scaled to CDFT. The P3MT pairs were generated as co-facial oriented, planar segments $\Delta x = 0$ Å or with a lateral shift about $\Delta x = 4$ Å for various distances $\Delta z = [3.0, 3.5, 4.0, 5.0, 6.0]$ Å.

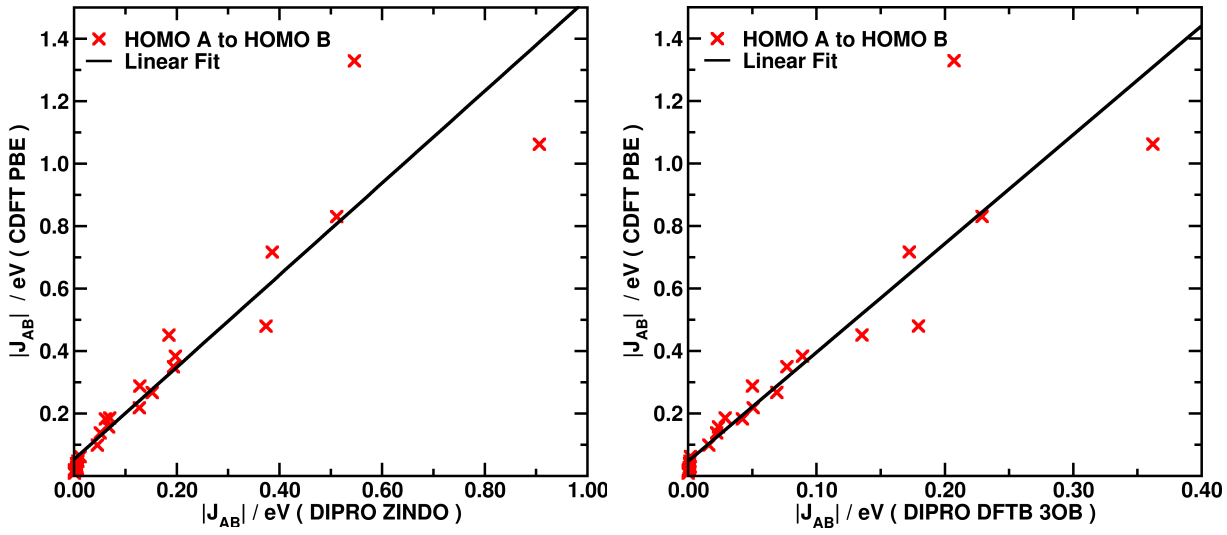

(a) (b)

Figure S4: Charge transfer integral $|J^{\mathrm{h}}_{\mathrm{AB}}|$ for hole transfer in P3MT pairs of $n = [3, 5, 7]$. The DIPRO method in conjugation with (a) ZINDO, and (b) DFTB/3OB-3-1 is scaled to CDFT/PBE/PW. The P3MT pairs are generated as co-facial oriented, planar segments $\Delta x = 0$ Å or with a lateral shift about $\Delta x = 4$ Å for various distances $\Delta z = [3.0, 3.5, 4.0, 5.0, 6.0]$Å.

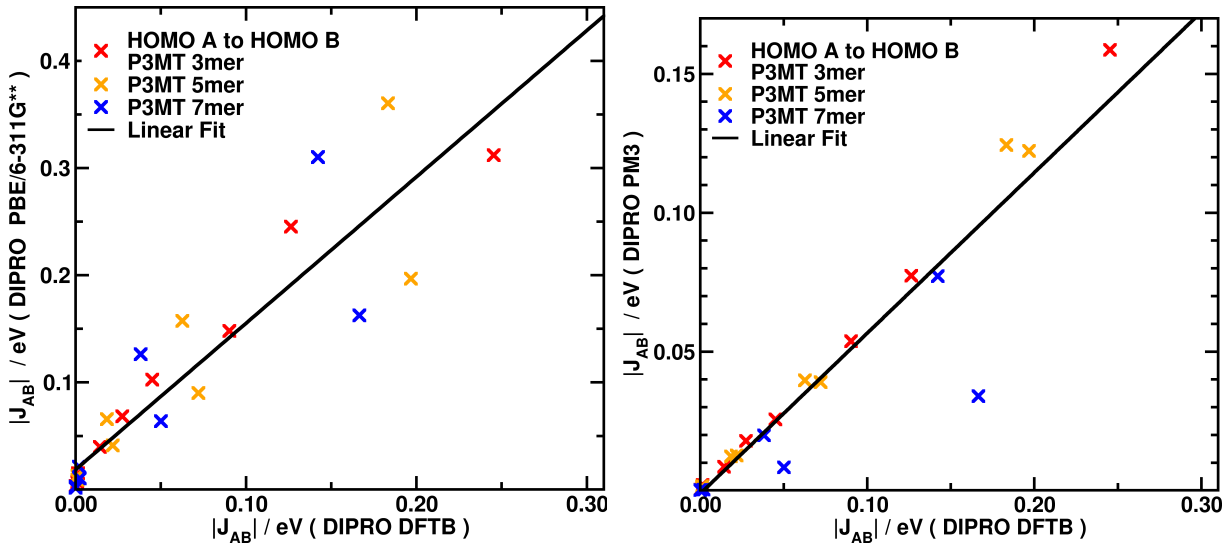

(a) (b)

Figure S5: Charge transfer integral $|J^{\mathrm{h}}_{\mathrm{AB}}|$ for hole transfer in P3MT pairs of $n = [3, 5, 7]$. The DIPRO/DFTB/Mio-1-1 data is scaled to (a) PBE/6-311G** and (b) PM3. The P3MT dimers are generated as planar segments with various distances [3.0,3.5,4.0,5.0,6.0] Å or with 3.0 Å and a lateral shift about 4 Å.

4 Charge transfer integral distribution in P3HT

The distributions of DIPRO charge transfer integrals can vary significantly in their shape, the average values and the standard deviation dependent on the underlaying semiempirical methods PM3, AM1, ZINDO and DFTB (Fig. S6). The mean values and standard deviations are listed in (Tab. S1).

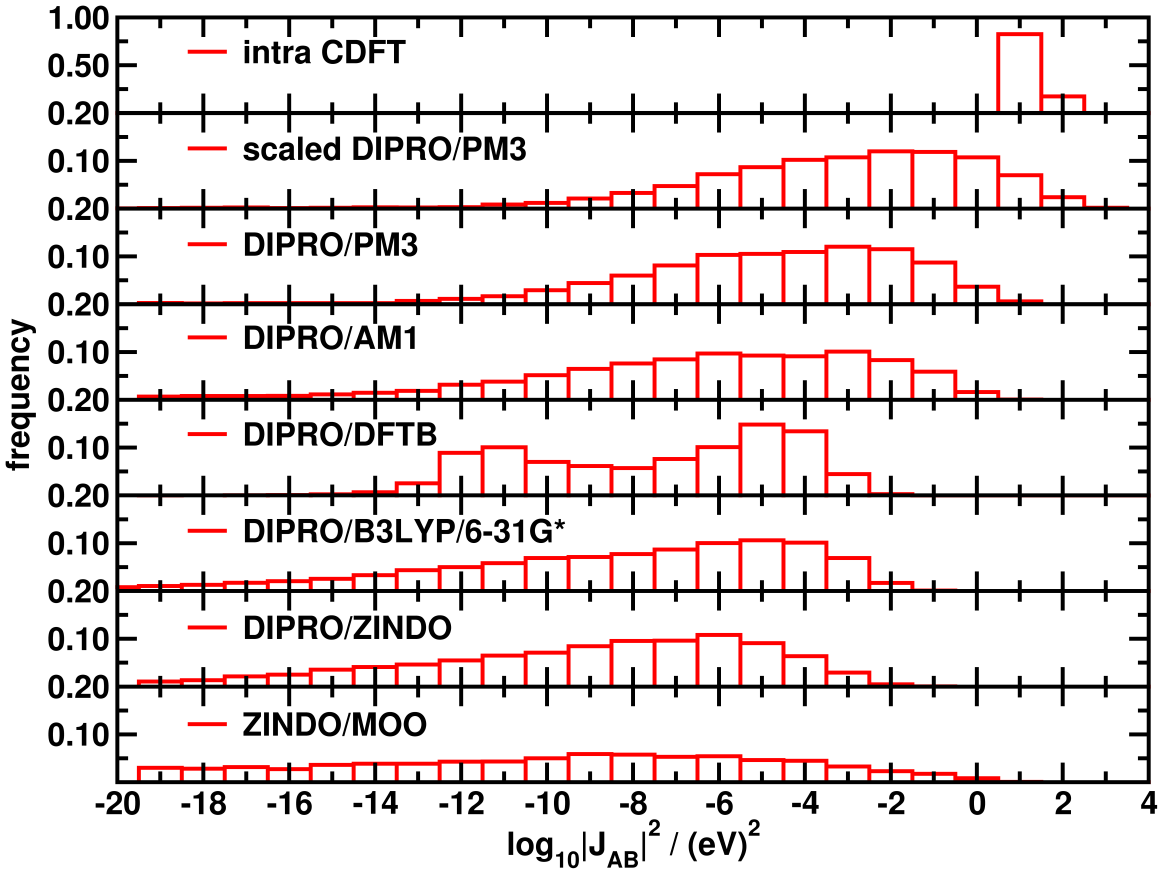

Figure S6: Distribution of the charge transfer integrals $|J_{\mathrm{AB}}|^2$ for hole transfer in an amorphous, segmented P3HT morphology using ZINDO/MOO or DIPRO in conjugation with DFTB/3OB or different semiempirical methods PM3, AM1, ZINDO.

Table S1: Mean values of the charge transfer integrals $\overline{\log_{10}|J_{AB}|^2}$ for hole transfer in an amorphous, segmented P3HT morphology using ZINDO/MOO or DIPRO in conjugation with DFTB/3OB or different semiempirical methods PM3, AM1, ZINDO.

method	$\log_{10}(\lvert J_{AB}\rvert^2/\mathrm{eV}^2)$
PM3	-6.38 ± 5.54
AM1	-7.58 ± 5.15
DFTB/3OB	-8.02± 3.07
ZINDO	-9.96±4.52
ZINDO/MOO	-14.15±8.79

5 Order parameter in P3HT

The order parameter S is defined as follows

$$S = \frac{3}{2}\left\langle (\overline{\mathbf{n}} \times \mathbf{n}_i)^2 - \frac{1}{3} \right\rangle, \tag{1}$$

where $\overline{\mathbf{n}}$ is the predominant direction vector. The vectors $\mathbf{n}_i$ are visually defined for every thiophene unit along the polymer chain with $n = 32$ segments (Fig. S7). For an isotropic phase S yields the value $S = 0$. It possesses the value $S = 1$ for the nematic phase and yields $S = -\frac{1}{2}$, if all $\mathbf{n}_i$ are orthogonal to $\overline{\mathbf{n}}$. The small values in the orientation parameter $S_{n_x} = 7.10 \times 10^{-4}$, $S_{n_y} = -9.42 \times 10^{-3}$ and $S_{n_z} = 1.25 \times 10^{-3}$ indicate the presence of P3HT in an amorphous phase.

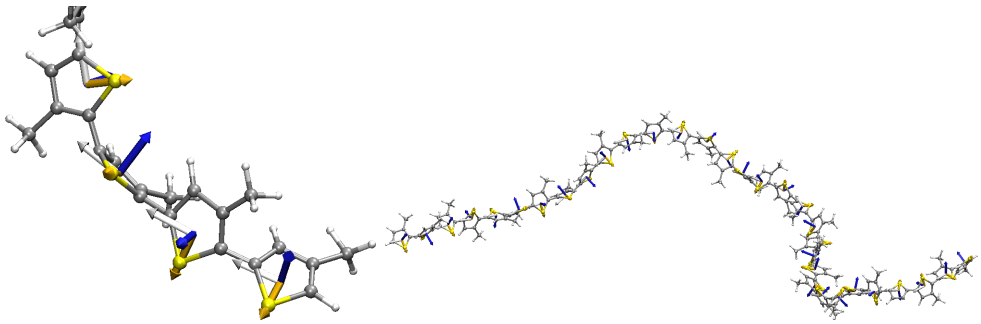

Figure S7: Visual representation of a local coordinate system in P3MT thiophene rings (left) and distribution along an entire P3MT 32mer chain (right). The origin of the local coordinate system is located at every center of mass of the thiophene rings. $\mathbf{n}_x$ (yellow) points towards the sulfur atom, $\mathbf{n}'_y$ in direction to the COM of the next thiophene ring. $\mathbf{n}_z$ (blue) is the orthonormal vector to the thiophene plane $\mathbf{n}_z = \mathbf{n}_x \otimes \mathbf{n}'_y$, which is spanned by $\mathbf{n}'_y$ and $\mathbf{n}_x$. Finally, we choose $\mathbf{n}_y = \mathbf{n}_x \otimes \mathbf{n}_z$ to guarantee the orthonormality.

6 Distributions of site energies and outer sphere reorganization energy

The site energy contributions $E_i = E^{\mathrm{el}} + E^{\mathrm{pol}}$ for 416 P3HT chains using the Thole model (Fig. S8) lead to an average energy $\overline{E}_{\mathrm{i}}^{\mathrm{h}} = (-0.131 \pm 0.146)$ eV for hole transport. Here, no partitioning of the P3HT polymer chains with segment length $n = 32$ is employed. Moreover, the outer sphere reorganization energy distribution is centered at $\overline{\lambda}_{\mathrm{out}}^{\mathrm{h}} = (0.157 \pm 0.014)$ eV for hole transport.

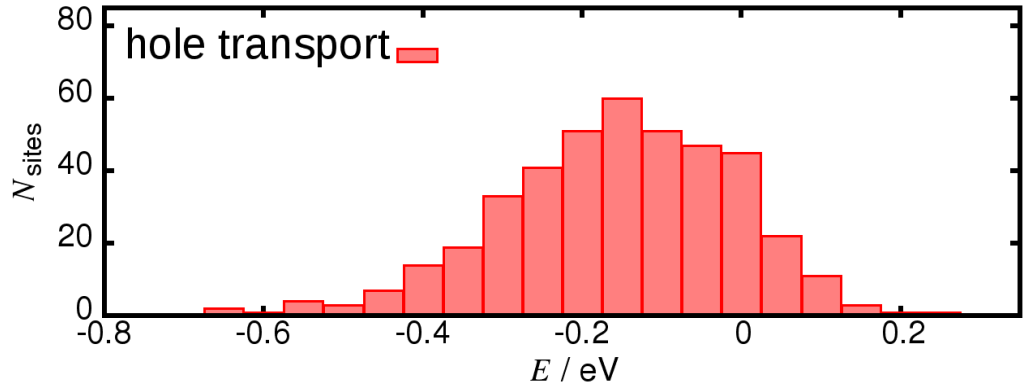

(a)

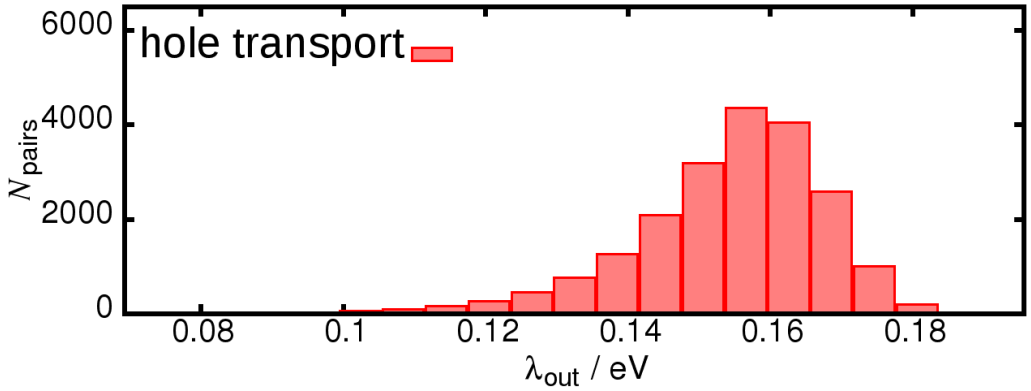

(b)

Figure S8: a) Distribution of site energy contributions $E_i = E^{\mathrm{el}} + E^{\mathrm{pol}}$ in P3HT $n = 32$ chain using the Thole model.
b) Distribution of the outer sphere reorganization energy λ^{out} for charge transfer pairs N_{pais} P3HT 32mer in a morphology with 416 P3HT chains.

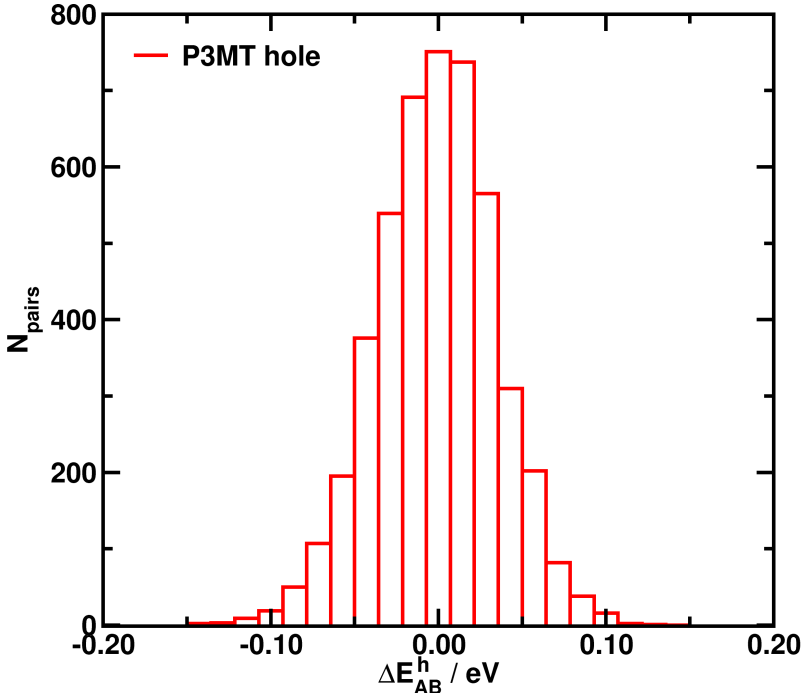

(a)

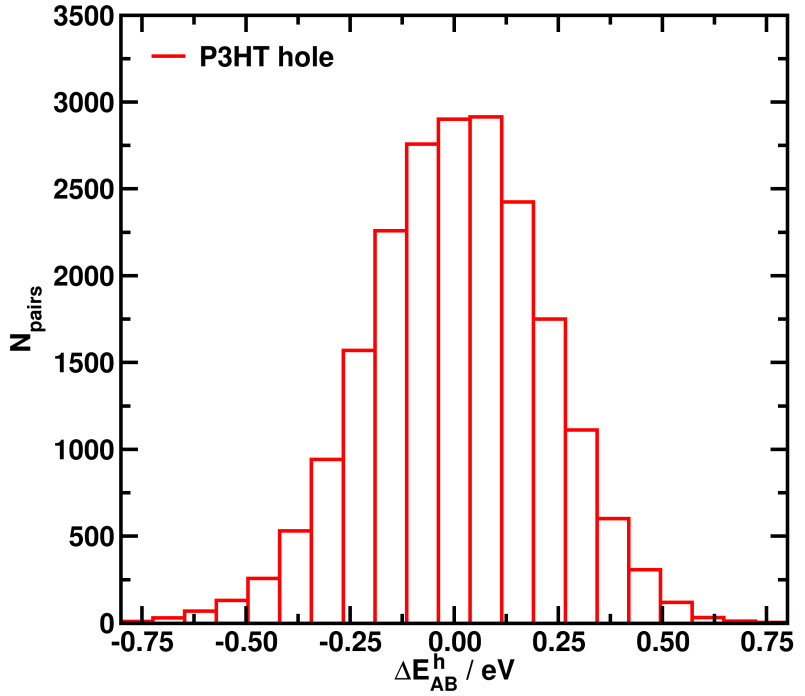

(b)

Figure S9: a) Distribution of site energy differences $\Delta E^{\mathrm{h}}_{\mathrm{AB}}$ (Eq. 5) in P3MT, and b) P3HT with thiophene segment length $n = 32$ using the Thole model in a morphology with 416 P3HT chains. P3HT yields a broader distribution $\Delta\overline{E}^{\mathrm{h}}_{\mathrm{AB}} = (0.0064 \pm 0.2099)$ eV when compared to P3MT $\Delta\overline{E}^{\mathrm{h}}_{\mathrm{AB}} = (0.00119 \pm 0.0354)$ eV.

7 P3HT polymer chain partitioning in amorphous phase

A pair of neighbouring P3MT polymer chains with chain segment length $n = 32$ is depicted in figure S10 as an outtakes from the DIPBI/P3HT morphology. The chains show two interchain junctions for a possible interchain charge transfer. One can see that the frontier orbitals like HOMO and LUMO are not delocalized along the entire polymer chain, but only localized on a number of tiophene subunits (Fig. S10,a,b). If one evaluates the charge transfer integral between the entire $n = 32$ polymer P3MT chains, one obtains only a significant value for hole transfer $|J^{\mathrm{h}}_{\mathrm{AB}}| = 1.97 \times 10^{-3}$ eV, as the HOMOs are localized for both monomers at the intermolecular junction site, whereas the charge transfer integral for electron transfer is negligible $|J^{\mathrm{e}}_{\mathrm{AB}}| = 2.05 \times 10^{-11}$ eV for a LUMO A to LUMO B transitions, as the involved orbitals are located far apart from each other. This finding is also reflected in the frontier orbital overlap for hole transfer $|S^{\mathrm{h}}_{\mathrm{AB}}| = 4.24 \times 10^{-4}$ and the corresponding tiny value for electron transfer $|S^{\mathrm{e}}_{\mathrm{AB}}| = 3.80 \times 10^{-12}$. Hence, the resulting DIPRO charge transfer integral for electron transfer and the associated Marcus rate drop to zero.

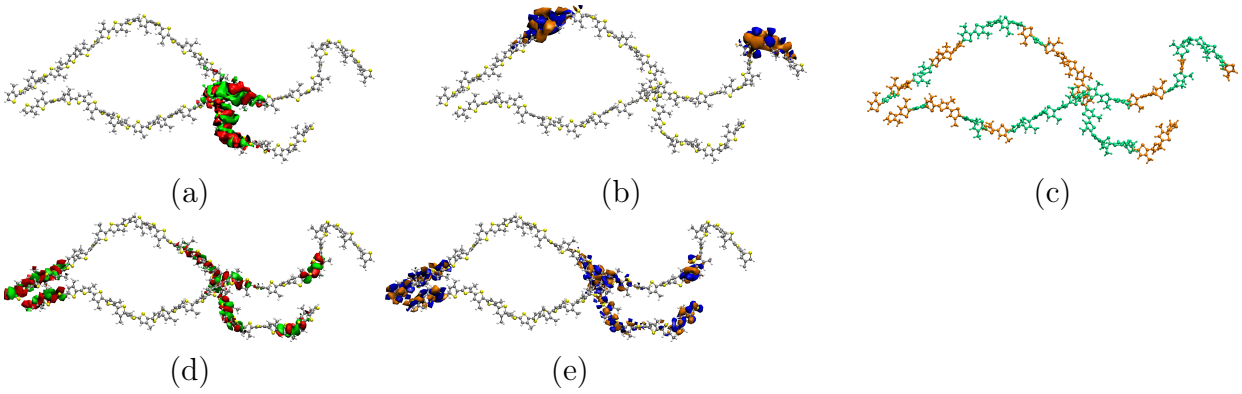

Figure S10: Localization of frontier orbitals at a pair of two P3MT chains with a segment length $n = 32$ for (a) the HOMO (red, green) and (b) the LUMO (blue, orange). Partitioning of two P3MT chains into segments (orange, cyan) at a cutoff angle $\theta^{\mathrm{cut}}_{\mathrm{SCCS}} = 75°$ (c). (d) Superposition of frontier orbitals HOMOs (red, green) and (e) LUMOs (blue, orange) of all segments involved in interchain transitions (B3LYP/6-31G*).

One can overcome this deficiency, if the polymer chain is partitioned into segments (Fig. S10,c). Therefore a cutoff dihedral angle $\theta^{\mathrm{cut}}_{\mathrm{SCCS}}$ between neigbouring SCCS atoms is introduced. This entails an a priori selection of the conjugated segments, that represent the hopping sites in the kMC simulations. Here, a cutoff dihedral angle $\theta^{\mathrm{cut}}_{\mathrm{SCCS}} = 75°$ is applied. The segments are saturated with virtual H atoms in the DIPRO calculations for the charge transfer integral, that incorporate the localization and shape of the DFT-based frontier orbital. The partitioning results in 12 and 13 conjugated segments at the first and second chain, respectively. The segment length is between $n = 1$ and 10 thiophene subuints. The HOMOs and LUMOs are located at the segments, which are in close proximity (Fig. S10,d,e) and the corresponding Marcus rates yield 9 possible interchain transitions with non-negligible contributions. Averaging all interchain transitions leads to

$|\overline{J}^{\mathrm{h}}_{\mathrm{AB}}| = (4.80 \pm 5.71) \times 10^{-3}$ eV for hole transfer and higher values for electron transfer $|\overline{J}^{\mathrm{e}}_{\mathrm{AB}}| = (1.76 \pm 2.80) \times 10^{-2}$ eV. This trend is also reflected in the averaged overlap $|\overline{S}^{\mathrm{h}}_{\mathrm{AB}}| = (6.58 \pm 9.62) \times 10^{-4}$ and $|\overline{S}^{\mathrm{e}}_{\mathrm{AB}}| = (1.97 \pm 2.91) \times 10^{-3}$.

Comparison of the frontier orbitals including the side chains in P3HT with partitioning (Fig. S11,a,b) yields a similar localization as for the P3MT polymer chains (Fig. S10,d,e), as the side chains do not affect the frontier orbital localization on the polymer backbone. Averaging all interchain transitions for the P3HT leads to $|\overline{J}^{\mathrm{h}}_{\mathrm{AB}}| = (5.26 \pm 8.58) \times 10^{-3}$ eV and $|\overline{J}^{\mathrm{e}}_{\mathrm{AB}}| = (1.71 \pm 2.80) \times 10^{-3}$ eV with DIPRO/B3LYP/6-31G*. The averaged overlap $|\overline{S}^{\mathrm{h}}_{\mathrm{AB}}| = (7.27 \pm 13.9) \times 10^{-4}$ for hole transfer and $|\overline{S}^{\mathrm{e}}_{\mathrm{AB}}| = (1.84 \pm 2.92) \times 10^{-3}$ for electron transfer.

The $|\overline{J}_{\mathrm{AB}}|$ and $|\overline{S}_{\mathrm{AB}}|$ in P3MT do not deviate significantly from the results in P3HT, which entails the validity of the reduction of the side chains to methyl groups in the evaluation of the charge transfer integral with DIPRO, which reduces computational costs significantly.

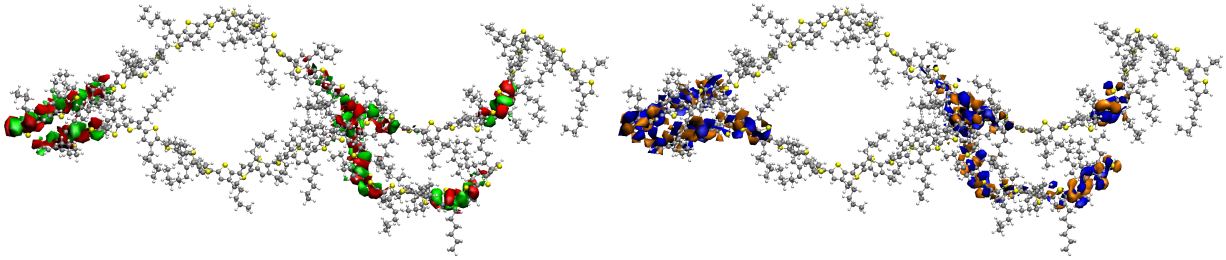

(a) (b)

Figure S11: Localization of frontier orbitals HOMOs (a) and LUMOs (b) involved in interchain transitions for a pair of P3HT chains including aliphatic side chains. The chains were extracted form the DIPBI/P3HT morphology partitioned into conjugated segments with $\theta^{\mathrm{cut}}_{\mathrm{SCCS}} = 75°$ (B3LYP/6-31G*). The reduction of the P3HT segment to a P3MT segment does not significantly alter the frontier orbital localization (See Fig. S10).

8 External field dependence in P3HT

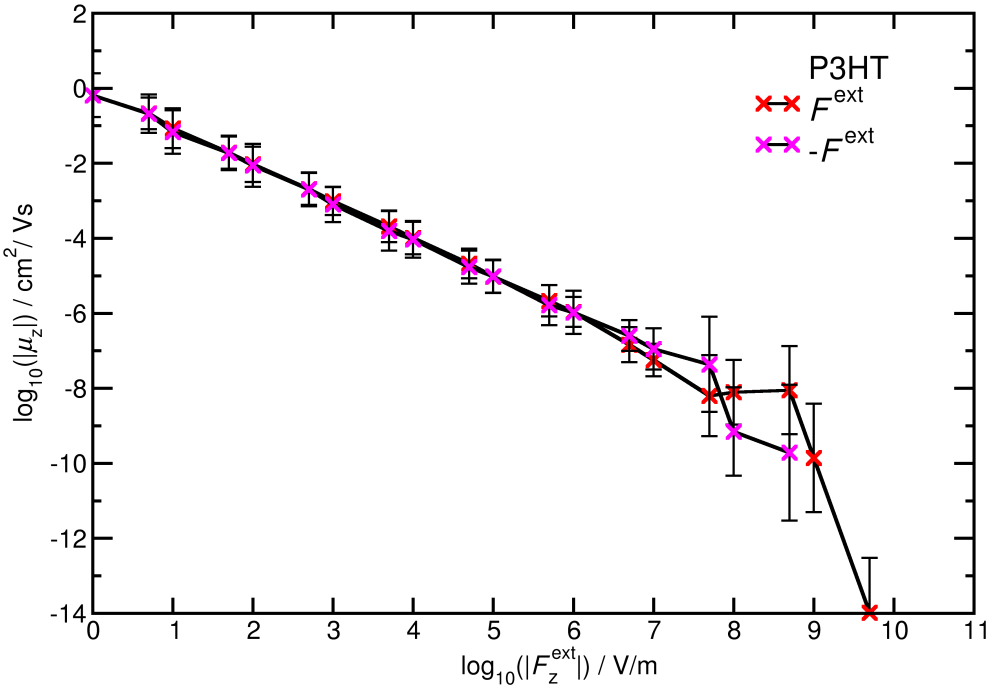

Figure S12: Field effect mobility μ_z for hole transport in P3HT morphology as a function of the external field F_z^{ext} from kinetic Monte Carlo simulations. If the external field is pointing in positive z direction, then the decadic logarithm of the external field has a positive sign and in the inverse case we employ a negative sign. Each kMC simulation has $N_{steps} = 1.0 \times 10^{10}$ steps, number of trajectories $N_{kmc} = 70$ per field strength.
The kMC simulations included CDFT-based intramolecular and DIPRO/PM3-based intermolecular hole transport, λ^{in}(B3LYP/6-311G*), $\lambda^{out} = 0.0$ eV, $\Delta E^{out} = 0.0$ eV.

9 Planarity descriptor for P3HT

We employ the planarity descriptor $P^\flat$, which takes all dihedral angles θ_i^{SCCS} into account between two neighboring thiophene units along a polymer chain [2].

$$P^\flat = \sum_i^{n-1} \frac{||\theta_i^{SCCS}| - 90|}{90} \quad \text{with } \theta_i^{SCCS} \in [-180, 180] \tag{2}$$

The descriptor $P^\flat$ is a measure of planarity. The contribution of a junction between two thiophene rings i with θ_i^{SCCS} to the total sum is zero, where the both rings are totally out of plane with each other and one where they are absolutely planar. The minimum value $P^\flat = 0$ indicates a completely broken conjugated π-system independent of the segment length n. The maximum value is $P^\flat = n - 1$, meaning that longer chains have the possibility to exhibit a higher measure of planarity.

The distributions for the planarity descriptor $P^\flat$ are depicted in Figure S13. The descriptor $P^\flat$ is determined individually for every P3HT chain with $n = 32$ and the distributions are compared for different P3HT:DIPBI morphologies from three different CG annealing protocols at 500 K, 700 K and 900 K. The histograms display three Gaussian distributions of $P^\flat$, which lead to the average values $\overline{P}^\flat_{\text{blend}} = 7.66 \pm 0.96$, 7.63 ± 0.93 and 7.75 ± 1.00 for the underlaying morphologies at 500 K, 700 K and 900 K, respectively. The $\overline{P}^\flat_{\text{blend}}$ are of similar magnitude, whereas the P3HT 32mers in the pristine P3HT yield a higher planarity $\overline{P}^\flat_{\text{P3HT}} = 17.95 \pm 1.07$.

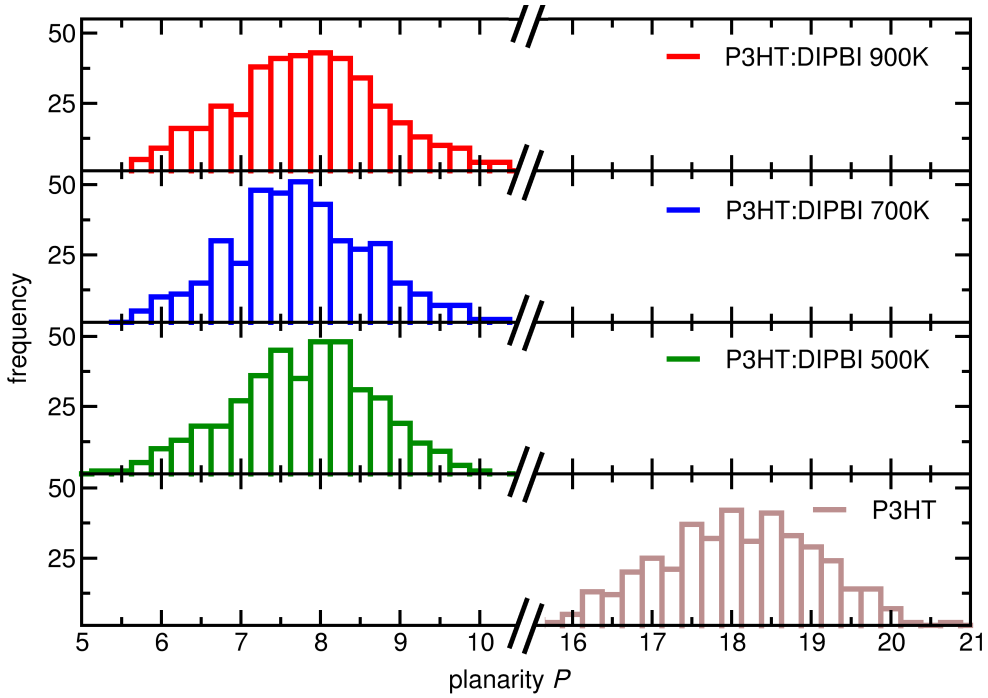

Figure S13: Distributions of the number of planarity descriptor $P^\flat$ for the P3HT 32mer inside the atomistic P3HT:DIPBI blend morphologies for three different CG annealing protocols [1] at 500 K, 700 K and 900 K and in amorphous P3HT for comparison.

10 DIPBI aggregation

In order to analyze the aggregation patterns of DIPBI in the three P3HT:DIPBI morphologies, we define a geometric center $\mathbf{d}_\text{A}$ for every DIPBI located in between two C atoms (see green dot and neighbouring C atoms (Fig. S14)) and define a molecular plane, which is given by four distance vectors $\mathbf{R}_1, \mathbf{R}_2, \mathbf{R}_3, \mathbf{R}_4$ and then we determine four associated normal vector $\mathbf{n}_i$.

$$\mathbf{n}_1 = \frac{\mathbf{R}_1 \times \mathbf{R}_2}{\mathbf{R}_1 \cdot \mathbf{R}_2}, \quad \mathbf{n}_2 = \frac{\mathbf{R}_2 \times \mathbf{R}_3}{\mathbf{R}_2 \cdot \mathbf{R}_3}, \quad \mathbf{n}_3 = \frac{\mathbf{R}_1 \times \mathbf{R}_4}{\mathbf{R}_1 \cdot \mathbf{R}_4}, \quad \mathbf{n}_4 = \frac{\mathbf{R}_3 \times \mathbf{R}_1}{\mathbf{R}_3 \cdot \mathbf{R}_1}, \tag{3}$$

The normal vector $\mathbf{n}_{\mathrm{A}}^{\mathrm{DIPBI}}$ is the average of these four normal vectors $\mathbf{n}_i$ as follows

$$\mathbf{n}_{\mathrm{A}}^{\mathrm{DIPBI}} = \frac{\sum_i^4 \mathbf{n}_i}{|\sum_i^4 \mathbf{n}_i|}. \tag{4}$$

A visual definition of the vectors $\mathbf{R}_1, \mathbf{R}_2, \mathbf{R}_3, \mathbf{R}_4$ and corresponding normal vector $\mathbf{n}_{\mathrm{A}}^{\mathrm{DIPBI}}$ is depicted in Figure S14 for a selected DIPBI (green vector).

We calculate the intermolecular distance $d_{\mathrm{AB}} = |\mathbf{d}_{\mathrm{B}} - \mathbf{d}_{\mathrm{A}}|$ and the enclosed angle $\alpha = \arccos(\mathbf{n}_{\mathrm{A}}^{\mathrm{DIPBI}} \cdot \mathbf{n}_{\mathrm{B}}^{\mathrm{DIPBI}})$ for every adjacent DIPBI molecule B in the vicinity of A ($r_{\mathrm{cut}} = 15$ Å) in order to characterize the relative orientation of two DIPBI molecules. The density plots demonstrate the frequency of occurrence of distinct relative DIPBI/DIPBI arrangements as a function of d_{AB} and α in the simulation box (Fig. S14).

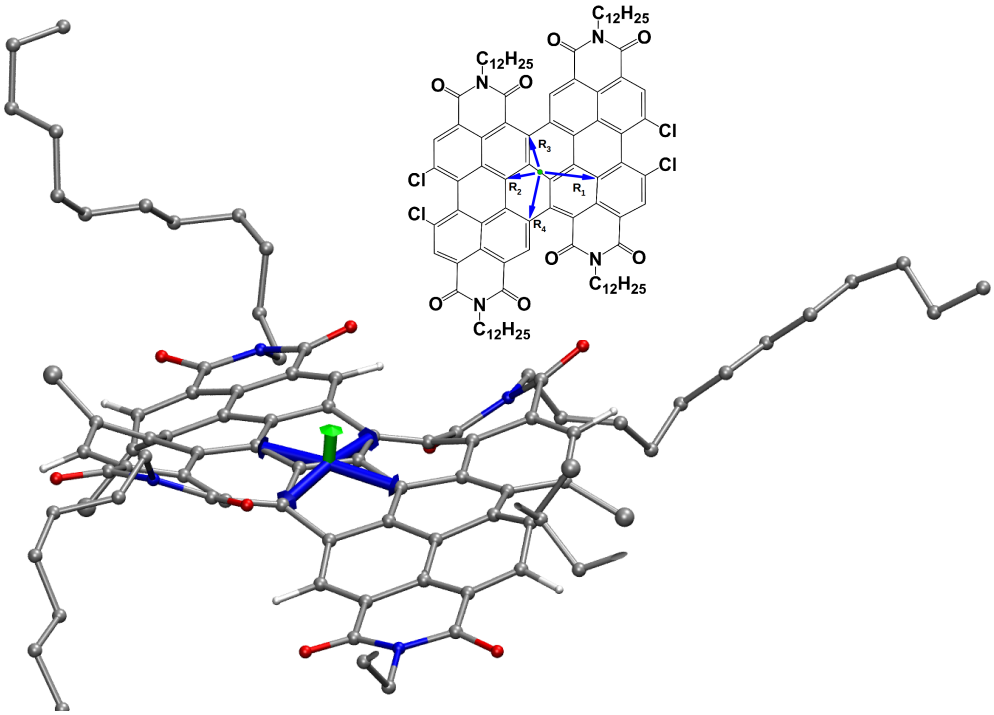

Figure S14: Selected DIPBI and normal vector $\mathbf{n}_{\mathrm{A}}^{\mathrm{DIPBI}}$ (green vector). The inset show the chemical structure and the vectors $\mathbf{R}_1, \mathbf{R}_2, \mathbf{R}_3, \mathbf{R}_4$ (blue vectors) pointing from the geometric center (green circle) to carbon atoms in the vicinity in order to define a molecular plane.

11 Radial distribution function

The radial distribution functions $g(r)$ of the hopping sites centers do not alter significantly, when comparing three different morphologies at three types of annealing temperatures 500K, 700K and 900K (Fig. S15). The function $g(r)$ takes DIPBI molecules and the P3HT hopping site centers after the segmentation with $\theta_{\mathrm{SCCS}}^{\mathrm{cut}} = 75°$ into account. It reveals a maximum at 3.65 Å to the nearest hopping neighbours, and higher order local maxima at 5.45 Å, 7.25 Å and 9.00 Å .

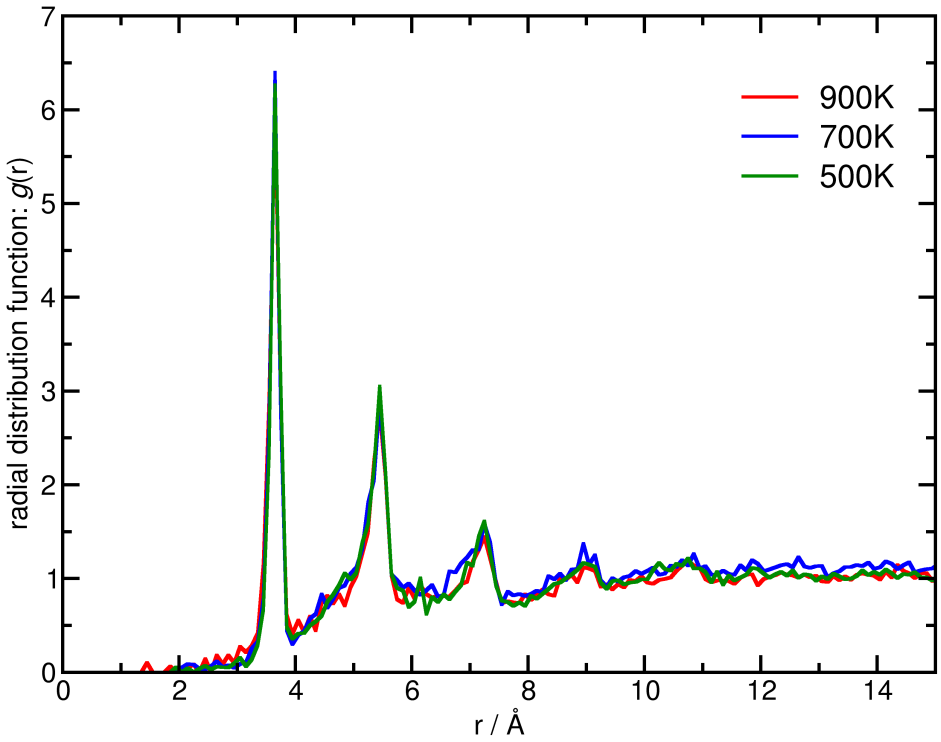

Figure S15: Radial distribution function $g(r)$ of the hopping sites centers for the P3HT:DIPBI blend after the polymer chain partitioning with $\theta^{\text{cut}}_{\text{SCCS}} = 75°$ in three different morphologies and CG annealing protocols at 500 K, 700 K and 900 K.

12 Escape rate

The average escape Marcus rate $\overline{k}^{\text{esc}}$ decays as a function of the thiophene segment length n (Fig. S16). The average hole escape rate from a DIPBI molecule exceeds the value of P3HT for hole transfer, which is in line with the expected donor / acceptor character of P3HT and DIPBI. Note the logarithmic scale and the large standard deviations. The outliers at $n = 14$ and 16 are attributed to missing statistics and local energetic disorder.

As the average resting time t^{r} is the inverse of the escape rate $\overline{k}^{\text{esc}}$, one finds an increasing resting time for longer thiophene segments.

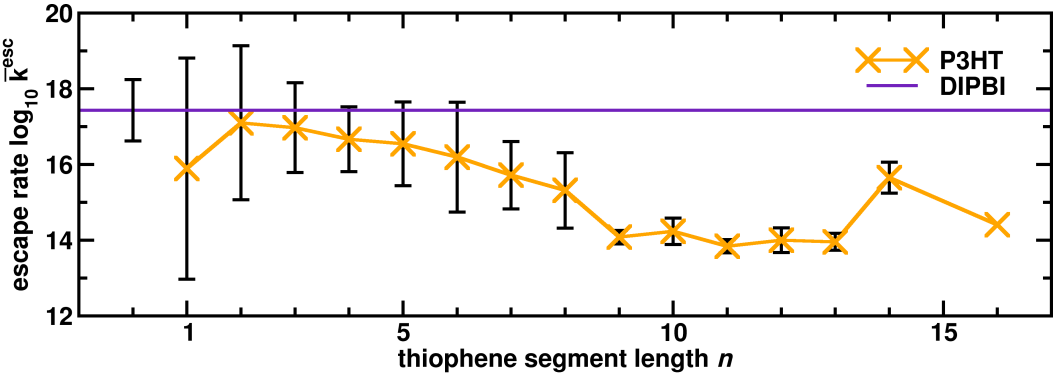

Figure S16: Decadic logarithm of the average escape Marcus rate $\log_{10} \overline{k}^{\mathrm{esc}}$ from hopping sites as a function of the thiophene segment length n of a conjugated segment in the P3HT:DIPBI morphology. The $\overline{k}^{\mathrm{esc}}$ for hole transfer include intermolecular and intramolecular transitions in P3HT. The average value for DIPBI is shown for comparison.

13 P3HT aggregation

The relative alignment of tiophene units in neighbouring thiophene chains is analyzed in density plots for the center of mass distances d_{AB} of individual thiophene rings with segment length $n = 1$ and as a function of the angle α between the corresponding normal vectors of the thiophene planes. Figure S17 displays the distributions for three P3HT:DIPBI morphologies with annealing temperatures at 500 K, 700 K and 900 K.

One can find a close parallel alignment of the thiophene units at a minimum distance about $d_{\mathrm{AB}} \approx 4$ Å a parallel alignment but a higher frequency of pairs with a $\alpha = [40°, 140°]$ with a non-parallel alignment at $d_{\mathrm{AB}} \approx 6$ Å. An increase in temperature results in a smearing of the distributions, as parallel aligned aggregation patterns dissolve.

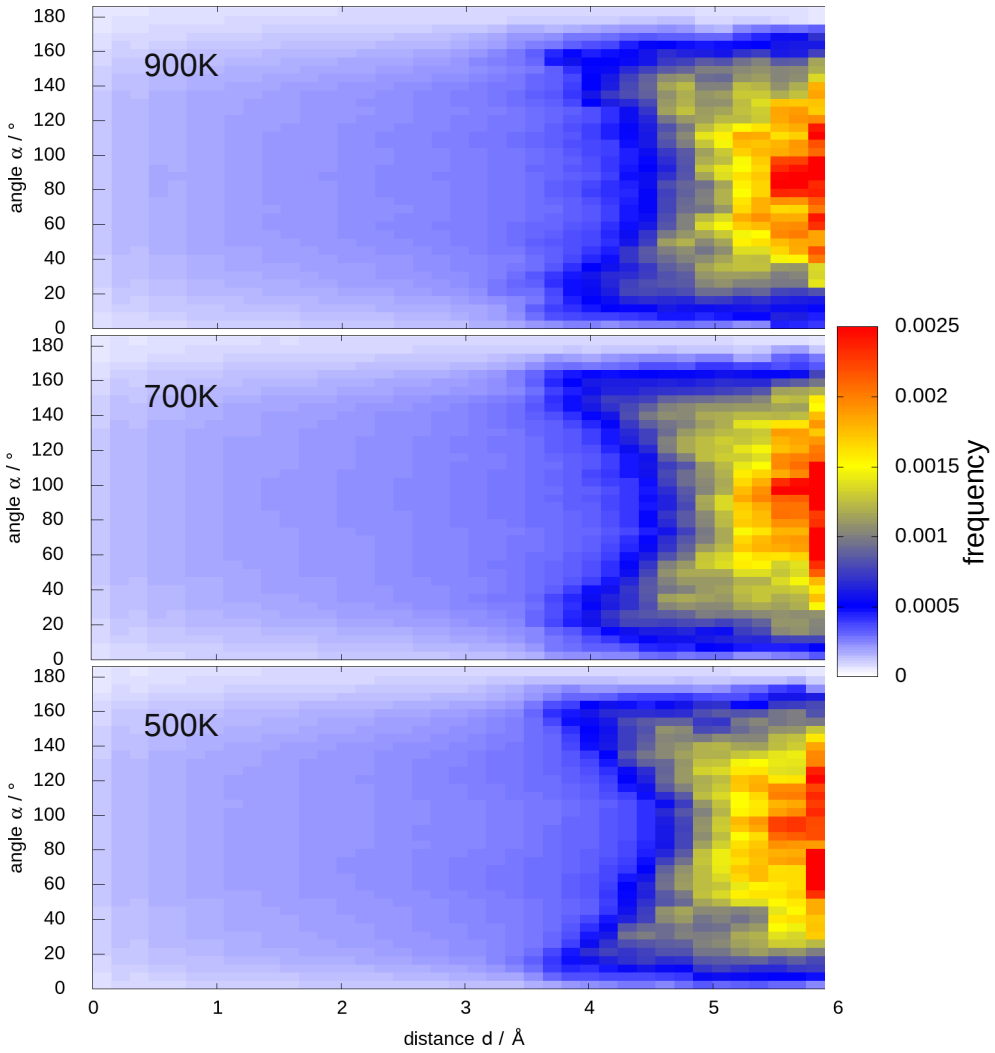

Figure S17: Density plots for the relative alignment of tiophene units in neighbouring thiophene chains as a function of the center of mass distances d_{AB} for individual thiophene rings with segment length $n = 1$ and the angle α between the corresponding normal vectors of the thiphene planes for three P3HT:DIPBI morphologies with annealing temperatures at 500 K, 700 K and 900 K.

14 Comparison P3MT and P3HT:DIPBI

In the following, we compare distributions for P3HT (Tab. S2,10) and P3HT:DIPBI morphology at 500 K (Tab. S2,15). The distributions contain data for both specimen in the blend. The Marcus rates for hole transfer are shifted to higher rates in P3HT:DIPBI when compared to pure P3HT (Fig. S18). The distribution of hopping site distances in pure P3HT is broader and centered at a higher value compared to the blend material (Fig. S20). The distributions of the occupation numbers are depicted in Figure S21. The distributions of local currents yield a tendency of higher currents in then blend P3HT:DIPBI than in pure P3HT (Fig. S22).

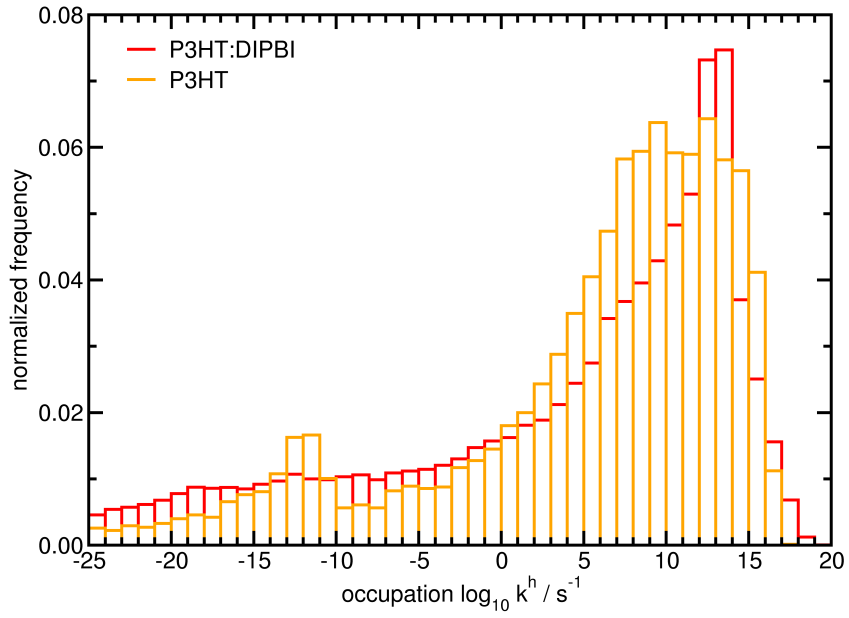

Figure S18: Distribution of Marcus hole transfer rates as the decadic logarithm $\log_{10} \overline{k}^{\mathrm{h}}$ in P3HT and in P3HT:DIPBI morphology at 500 K.

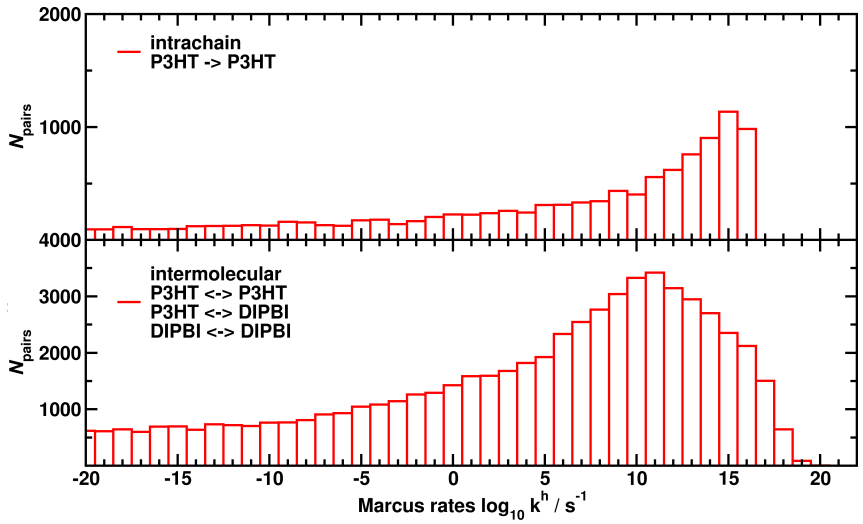

Figure S19: Distribution of intra- and intermolecular Marcus hole transfer rates as the decadic logarithm $\log_{10} \overline{k}^{\mathrm{h}}$ in P3HT:DIPBI morphology at 500 K.

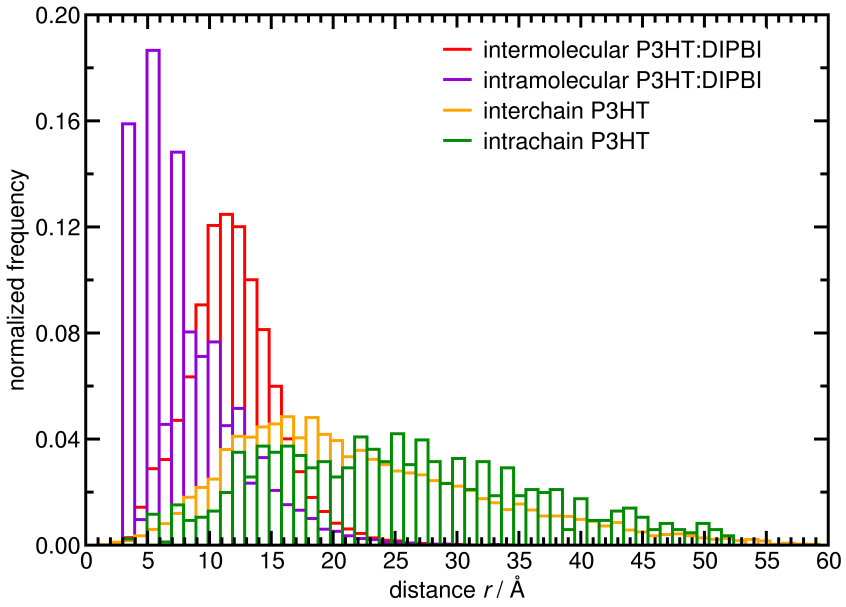

Figure S20: Distribution of hopping site distances d_{ij} in P3HT and in P3HT:DIPBI morphology at 500 K.

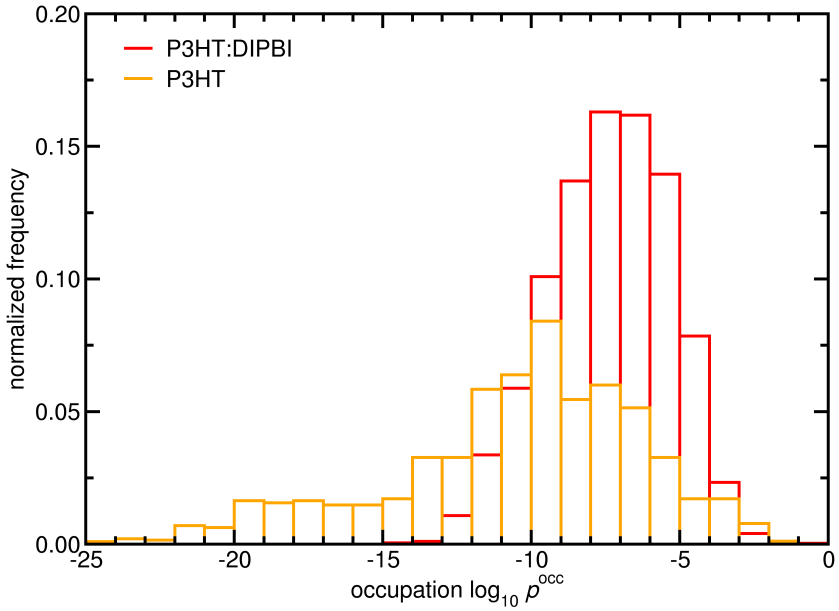

Figure S21: Distribution of occupation numbers p^{occ} in P3HT and in P3HT:DIPBI morphology at 500 K.

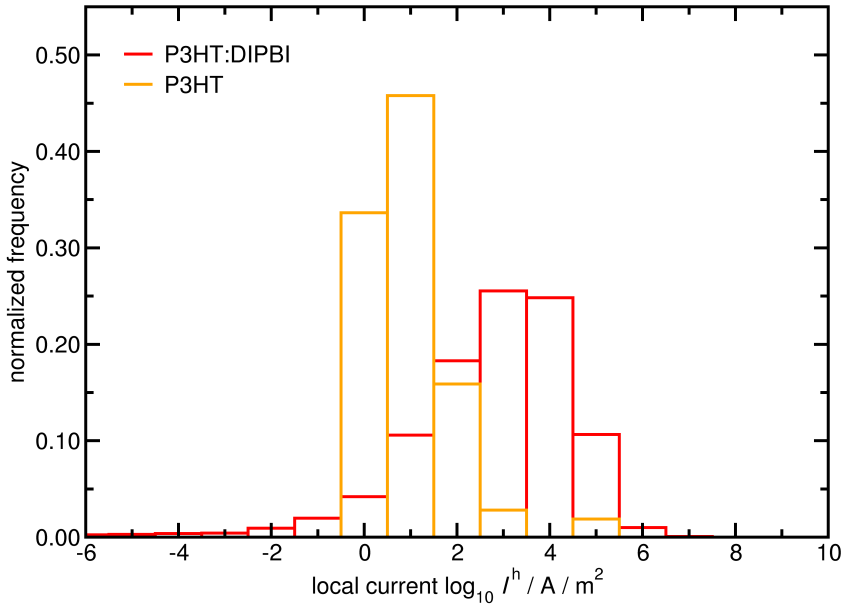

Figure S22: Distribution of local hole currents $\log_{10} I^{\mathrm{h}}$ based on kMC simulations of hole transport in P3HT and P3HT:DIPBI morphology at 500 K.

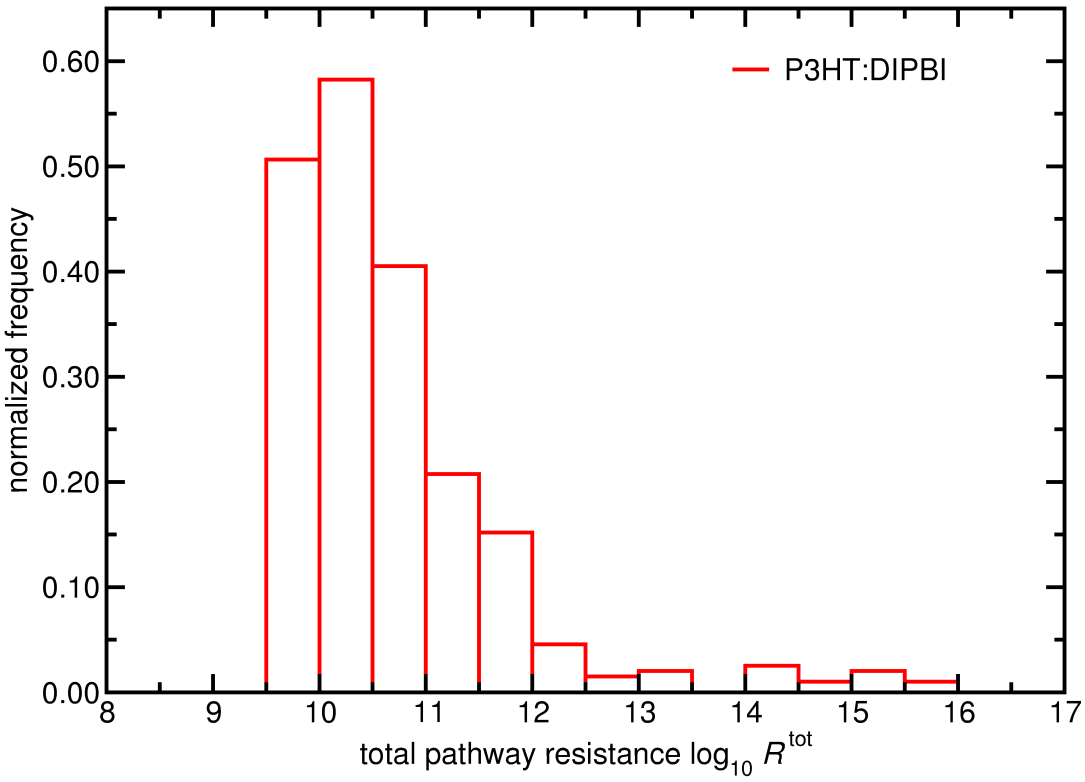

Figure S23: Distribution of the total resistance $\log_{10} R^{\mathrm{tot}}$ for hole transport pathways in P3HT:DIPBI morphology using the Dijkstra algorithm.

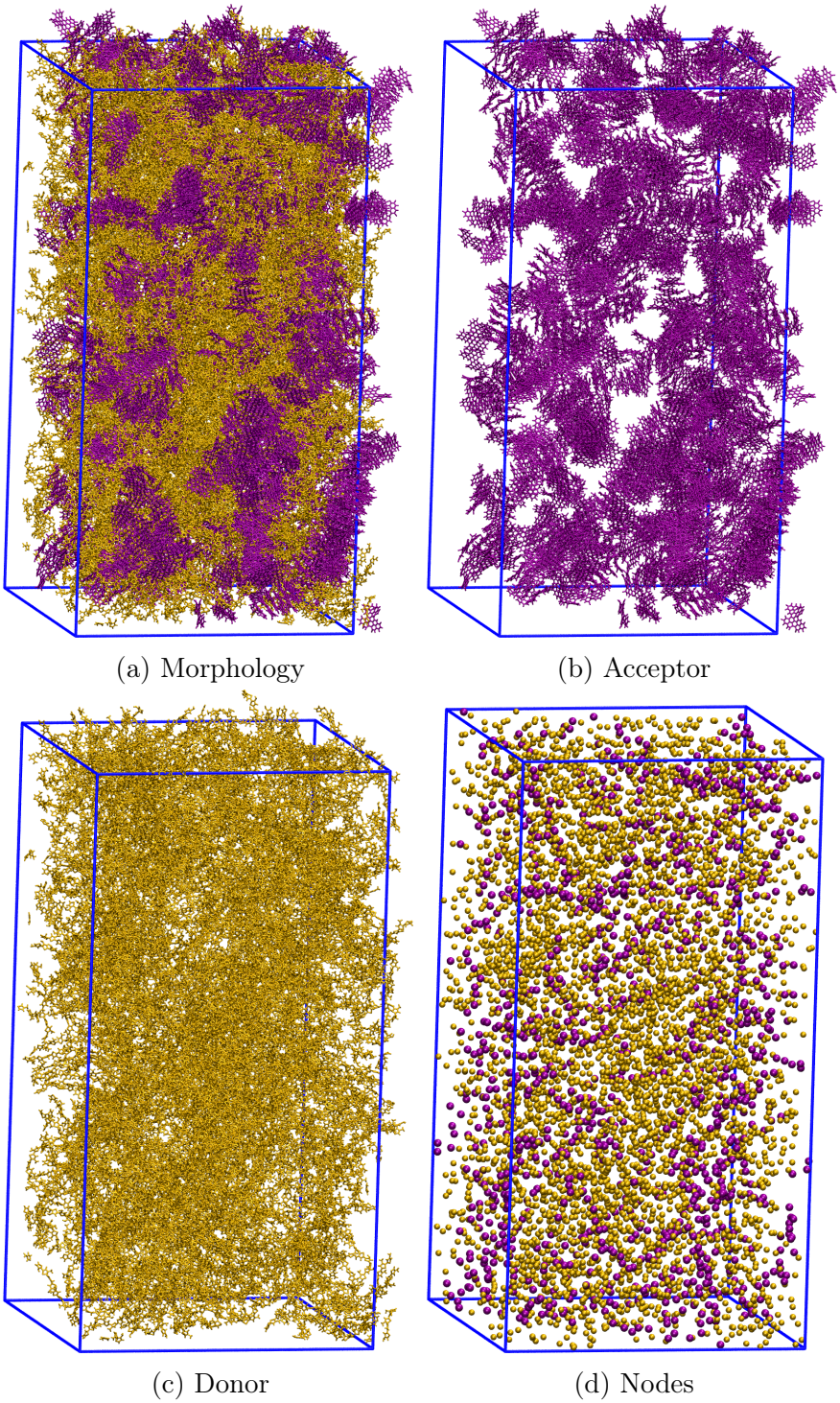

(a) Morphology (b) Acceptor

(c) Donor (d) Nodes

Figure S24: (a) P3HT:DIPBI blend morphology equilibrated at an annealing temperature 500 K. (b) Domains of the acceptor molecule DIPBI. (c) Domains of the donor polymer P3HT. (d) Distribution of hopping sites.

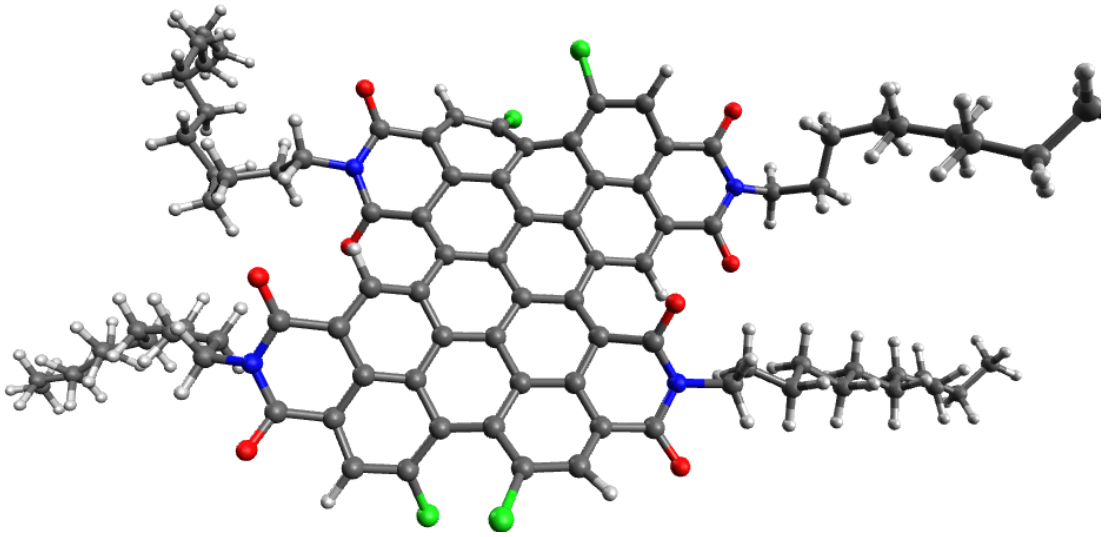

Figure S25: Optimized DIPBI structure in the electronic ground state S_0 according to PBE0-D3(BJ)/6-31G*

15 hole mobilities

Table S2: Collection of kMC simulations for various systems, methods for the charge transfer integral for intramolecular $|J_{\mathrm{AB}}^{\mathrm{intra}}|$ and intermolecular$|J_{\mathrm{AB}}^{\mathrm{inter}}|$ transport, the internal reorganization energies λ^{in} and site energy difference ΔE^{in} is evaluated on B3LYP/6-311G* level of theory. Outer-sphere contributions λ^{out}, ΔE^{out} are included for the entire polymer chain (32mer), including additional hydrogen atoms for segment saturation at the inter-segment linking positions (add H) or (no H). They can be treated as virtual sites (virt. H) or not virtual H (no virt. H). The polymer chains are segmented $\theta_{\mathrm{SCCS}}^{\mathrm{cut}} = 75°$ (seg) or remain complete $n = 32$ for the entire chain (32mer). The resulting hole mobility μ_{tot} and the standard deviation σ_{tot} are displayed in [cm^2/Vs]. We include all rates to the 12 nearest neighbours except in calculations (1) and (2), where we use neighbours within a spherical cutoff of 5 nm and 3 nm, respectively.

No	system	$\lvert J_{\mathrm{AB}}^{\mathrm{intra}}\rvert$	$\lvert J_{\mathrm{AB}}^{\mathrm{inter}}\rvert$	λ^{out}	ΔE^{out}	μ_{tot}	σ_{tot}
1	P3HT 32mer	—	ZINDO/MOO	32mer	32mer	1.73E-14	4.04E-14
2	P3HT (seg)	—	ZINDO/MOO	add H, virt. H	add H, virt. H	6.21E-09	6.62E-10
3	P3HT (seg)	CDFT	ZINDO/MOO	no H	add H, no virt. H	9.01E-08	4.70E-07
4	P3HT (seg)	CDFT	DIPRO/ZINDO	no H	add H, no virt. H	1.34E-12	7.76E-12
5	P3HT (seg)	CDFT	DIPRO/DFTB/3OB	no H	add H, no virt. H	5.41E-11	1.19E-10
6	P3HT (seg)	CDFT	DIPRO/AM1	no H	add H, no virt. H	1.84E-09	2.46E-10
7	P3HT (seg)	CDFT	DIPRO/PM3	no H	add H, no virt. H	1.85E-09	1.36E-08
8	P3HT (seg)	CDFT	DFTB/3OB scaled to CDFT	no H	add H, no virt. H	1.15E-09	4.77E-10
9	P3HT (seg)	CDFT	PM3 scaled to CDFT	no H	add H, no virt. H	3.81E-08	8.18E-08
10	P3HT (seg)	CDFT	PM3 scaled to CDFT	32mer	32mer	1.17E-03	3.14E-06
11	P3HT (seg)	CDFT	DIPRO/PM3	0	0	1.87E-07	4.00E-07
12	P3HT:DIPBI 500K (seg)	CDFT	DIPRO/PM3	0	0	6.02E-03	5.18E-05
13	P3HT:DIPBI 500K (seg)	CDFT	DIPRO/PM3	32mer	0	2.60E-07	6.09E-09
14	P3HT:DIPBI 500K (seg)	CDFT	DIPRO/PM3	32mer	32mer	3.07E-07	7.90E-09
15	P3HT:DIPBI 500K (seg)	CDFT	PM3 scaled to CDFT	32mer	32mer	8.41E-03	7.18E-05
16	P3HT:DIPBI 700K (seg)	CDFT	DIPRO/PM3	32mer	32mer	2.58E-07	1.39E-08
17	P3HT:DIPBI 900K (seg)	CDFT	DIPRO/PM3	32mer	32mer	5.27E-08	1.49E-09
18	P3HT:DIPBI 500K (seg)	CDFT	DIPRO/PM3	no H	add H, virt. H	6.15E-03	5.33E-04

Table S3: Comparison of three P3HT:DIPBI morphologies based on different annealing temperatures 500 K, 700 K, and 900 K. The number of hopping sites and charge transfer (CT) pairs for intermolecular and intramolecular transitions are listed including the 12 nearest neighbours (NN). The P3HT polymer chains are partitioned using $\theta^{\mathrm{cut}}_{\mathrm{SCCS}} = 75°$. Average hopping site distance $\overline{d}_{\mathrm{AB}}$ taking all transitions into account, and an average distance of the 12th nearest neighbour $\overline{d}_{\mathrm{NN12}}$ for all sites and around DIPBI molecules $\overline{d}^{\mathrm{DIPBI}}_{\mathrm{NN12}}$ and P3HT segments $\overline{d}^{\mathrm{P3HT}}_{\mathrm{NN12}}$.

	morphologies		
	500 K	700 K	900 K
hopping sites	6515	6575	6457
DIPBI molecules	1248	1248	1248
P3HT segments	5267	5327	5209
total number of CT pairs	47546	47869	47126
DIPBI↔DIPBI	3496	3544	2097
DIPBI↔P3HT	8726	8687	11290
P3HT↔P3HT	35324	35638	33739
P3HT↔P3HT intramolecular	4851	4911	4793
P3HT↔P3HT intermolecular	30473	30727	28946
All intermolecular CT pairs	42695	42958	42333
$\overline{d}_{\mathrm{AB}}$ [Å]	8.42 ± 3.07	8.38 ± 3.20	8.51 ± 3.10
$\overline{d}_{\mathrm{NN12}}$ [Å]	11.49 ± 2.11	11.46 ± 2.43	11.61 ± 2.01
$\overline{d}^{\mathrm{DIPBI}}_{\mathrm{NN12}}$ [Å]	14.21 ± 1.51	15.10 ± 1.71	14.19 ± 1.44
$\overline{d}^{\mathrm{P3HT}}_{\mathrm{NN12}}$ [Å]	10.80 ± 1.57	10.61 ± 1.57	11.03 ± 1.60

References

[1] "P3HT:DIPBI bulk heterojunction solar cells: morphology and electronic structure probed by multiscale simulation and UV/vis spectroscopy", T. Winands, M. Böckmann, T. Schemme, P.-M. T. Ly, D. H. de Jong, Z. Wang, C. Denz, A. Heuer, and N. L. Doltsinis, *Phys. Chem. Chem. Phys.* **18**, 6217–6227 (2016).

[2] "Toward a Molecular Understanding of the Detection of Amyloid Proteins with Flexible Conjugated Oligothiophenes", J. Sjöqvist, J. Maria, R. A. Simon, M. Linares, P. Norman, K. P. R. Nilsson, and M. Lindgren, *J. Phys. Chem. A* **118**, 9820–9827 (2014).